Supplementary Information for

Fibre Tapering Using Plasmonic Microheaters and Deformation-Induced Pull

Qiannan Jia, Weiwei Tang*, Wei Yan* and Min Qiu*

*Corresponding authors. Email: tangweiwei@ucas.ac.cn; wyanzju@gmail.com; qiu_lab@westlake.edu.cn

The PDF file includes:

Other Supplementary Information for this manuscript includes:

Movie S1: Ablation of the gold plate before the initiation of the fibre tapering process (corresponding to the system in Fig. 1B and C)

Movie S2: In-situ fibre tapering inside SEM (corresponding to Fig. 1B and C)

Movie S3: Spiral locomotion of the gold plate with input supercontinuum light source at low repetition rate (20 Hz-20 kHz)

Movie S4: Fibre tapering with modulated CW light at 1 Hz (scale bar = 10 μm)

Movie S5: Controllable fibre tapering with interventions of light source (supercontinuum light source, 100 kHz repetition rate)

Movie S6: Fabrication of a fibre taper with a topological insulator plate (supercontinuum light source, 100 kHz repetition rate)

Movie S7: Fabrication of a fibre taper with an amorphous gold plate (supercontinuum light source, 100 kHz repetition rate)

Movie S8: Liquid-like behavior of fibre probes with plasmonic heat

Movie S9: Evolution of the normal stress inside the fibre with prescribed displacement

Movie S10: Shift of the fibre loop in the attempt to release the inner stress

Section S1. Fibre tapering using modulated CW light source at 532 nm

Figure 4A in the main text shows that, with the input light being modulated continuous wave (1 Hz) at wavelength of 532 nm, the opto-thermal effect of the gold plate is sufficient to heat the fibre to above its softening temperature. It is thus reasonable to assume that this light source can also be used for fibre tapering in our experiment.

We successfully fabricated fibre tapers with amplitude-modulated CW light at 1 Hz repetition rate. SEM images of the plate-fibre system before and after the fibre tapering process are displayed in Fig. S4A and B. The initial diameter of the pre-tapered fibre is 2.55 μm, and the waist diameter of the resultant fibre taper is 960 nm. The recorded video of the tapering process is in Movie S4, where the fibre is gradually drawn thin with a speed synchronizing the modulation signal. Before the input light power reaches a certain level (~10 mW, dependent on the system configuration), neither ablation of the gold plate nor the softening of the fibre could be observed. Instead, periodic expansion and contraction of the gold plate could be inspected clearly, due to the periodically deposited heat. After the threshold power is reached, however, the gold plate would collapse and stick to the fibre, which serves as a static heater for the fibre tapering process that follows.

In simulation models, input CW light (without modulation) is associated with a steady-state heat transfer process. Fig. S4C shows the steady-state temperature profile (based on the calculated absorption profile in Fig. S3D) of a plate-fibre system with 20 mW input power. When modulated at a low repetition rate, the plate fibre system would enter a quasi-stationary regime, where the temperature of the system would quickly flatten and exhibit little difference between consecutive heating periods, as is demonstrated in Fig. S4D. The main difference between the stationary and quasi-stationary regimes with the same peak power is at the rising and falling edges of the heat load, where in the latter case, the current steady state is interrupted and the system is forced to restabilize into a new steady state. Besides, in contrast to the heat accumulation scheme of a high-repetition-rate pulsed load, temperature evolution with a modulated CW heat load shows zero overlap between the cooling edge of the current heat pulse and the rising edge of the next one. The mutual independency of heat pulses relies on the extended cooling window (0.5 s pulse interval for 1 Hz modulation speed), which allows the thermal system to relax completely. On the other hand, however, overlap does exist in the spatial space, where the temperature responses probed at different positions of the plate-fibre system (within 40 μm length) shows nearly identical tendency and slope. Approximately, heat can diffuse ~ 100 μm within 0.01 s with the thermal diffusivity of fused silica being $10^{-6}\ m^2 s^{-1}$. Therefore, the relative temperature uniformity could be reached at a speed beyond the temporal resolution of the heat input, and the time required for the heat to transfer among different probed points would become negligible.

Theoretically, modulated CW light could be used to fabricate fibre tapers. However, in experiments, fibres would break more easily and abruptly even with the heat source intervention (to turn off the light source), which we attribute to the thermal fatigue the fibre material experiences with periodic heat load. Unmodulated CW input is

admittedly the optimum choice to achieve steady and gradual heat deposition. Here we only use the modulated source to demonstrate the feasibility (to effectively heat the target and initiate phase transition) rather than practicality.

Section S2. Numerical simulations for opto-thermal effects in the fibre-plate system

2.1 Electromagnetic simulation

We perform electromagnetic simulation using the commercialized software Lumerical FDTD solutions. The input light modes supported by the pre-tapered fibre is calculated with the built-in mode source option. Here we only consider fundamental $HE_{11}^{verticle}$ mode (E field component predominantly perpendicular to the gold plate) and $HE_{11}^{horizontal}$ mode (E field component predominantly parallel to the gold plate). Spatial profile of light absorption is calculated based on the distribution of electric field, following the relation:

$$P_{abs} = 0.5 \cdot \varepsilon_0 \cdot Im(\varepsilon) \cdot \omega \cdot |E|^2 \quad (1)$$

(P_{abs}: absorption volume density,ε_0:vacuum permittivity, $Im(\varepsilon)$: imaginary part of relative permittivity, ω:angular frequency of the incident light, $|E|$:electric field magnitude).

The absorption spectrum is obtained by sweeping the incident wavelength within the bandwidth range of the supercontinuum light source (400-2400 nm).

To showcase the dependence of the absorption profile on the specific configuration of the plate-fibre system, we used well-defined rectangular gold plates and calculated the E-field distribution in corresponding systems. For simplicity, we set one side of the gold plate to be parallel to the fibre axis and change the incident wavelength (532 nm, 800 nm, 1 μm) and the contact length (30 μm, 45 μm). Schematic of the simulation set-up and the calculation results can be seen in Fig. S3.

2.2 Heat transfer simulation (static governing equation and transient equation)

Temperature distribution in the steady state regime is first simulated using the heat transfer module in Comsol Multiphysics. The absorption profile of the gold plate is imported from the calculation results in FDTD as the domain heat source. Given that radiation is the dominant channel for heat outflow at elevated temperatures (> 1000 K), surface-to-radiation boundary condition is imposed on all exterior boundaries (without which the calculated results would present an extra temperature rise of several hundred Kelvins). We assume that the temperature inside the SEM chamber is kept constant at 293.15 K. Therefore, the radiation outflow from the fibre-plate system can be calculated as:

$$-\boldsymbol{n} \cdot \boldsymbol{q} = \varepsilon\sigma(T_{amb}^4 - T^4) \quad (2)$$

($\boldsymbol{n}$: outward normal of the radiation surface, $\boldsymbol{q}$: heat flux arising from thermal radiation, ε: surface emissivity of corresponding materials, T_{amb}: reference temperature set at 293.15 K, T: Temperature of the discrete surface element)

Since fused silica possesses large surface emissivity (~0.9) compared to that of gold (~0.03), it can be inferred that at elevated temperatures, the heated region of the fibre contributes mostly to the radiation outflow in the whole fibre-plate system.

As for the transient calculation, it inherits all settings used in the steady-state regime, except that the domain heat source becomes time-variant. Apart from the spatial profile deduced from the absorption distribution, a pulsed temporal term is added to the heat source expression in the form of a Gaussian function:

$$Q(r,t) = P_{abs}(r) \cdot P_0 \cdot (\sqrt{\pi} \cdot \tau)^{-1} \cdot e^{-(t-t_0)^2/\tau^2} \quad (3)$$

($Q(r,t)$:spatially and temporally dependent domain heat source, P_{abs}: absorption volume density, P_0: single pulse energy, $(\sqrt{\pi} \cdot \tau)^{-1}$: normalizing coefficient for the Gaussian function, t_0: time delay of the pulse peak, τ: time constant of the pulsed signal)

The temporal heat transfer equation containing a time derivative term is solved in the time-dependent regime:

$$\rho c_p \frac{\partial T}{\partial t} + \nabla \cdot \boldsymbol{q} = Q(r,t) \quad (4)$$

(ρ: mass density of corresponding materials, c_p: heat capacity at constant pressure, $\boldsymbol{q}$: heat flux arising from both heat conduction and thermal radiation. For heat conduction, $\boldsymbol{q} = -k\nabla T$ with k being the thermal conductivity. For thermal radiation, $-\boldsymbol{n} \cdot \boldsymbol{q} = \varepsilon\sigma(T_{amb}^4 - T^4)$ is imposed on the outer surfaces of the plate and the fibre, as is the case for Eq. (2))

In order to derive the temperature response of the system to multiple consecutive pulses as in Fig. 5D, the temporal term of the heat source is set as a periodic function with a period of $\frac{1}{f_{rep}}$, where f_{rep} denotes the repetition frequency of the light source.

Since a modulated CW source (532nm) is used in experiments, we also conducted the heat transfer simulation to quantify the pattern of heat accumulation where the heat load is applied in a square wave fashion. The modulation frequency is set at 1 Hz and the duty ratio being 50%. The corresponding time-dependent temperature evolution is plotted in Fig S4D. Note that the heat source of this heat transfer simulation is directly derived from the E-field result in Fig. S3 using Eq. (1) and (3).

2.3 Convergence test for the fibre length in the heat transfer simulation model

The pre-tapered fibres used in the experiments possess uniform waist regions of a-few-millimetre length and evolve adiabatically along the transition region. It would be computationally expensive to establish a full-scale model strictly in accordance with the experiment, especially given the scale difference between the micro-plate and the fibre with a macro longitudinal dimension. Therefore, we simulate the pre-tapered fibre with a silica cylinder that mimics only the shape of the fibre waist region. Considering that the heat conduction (the heat convection is weak in the high vacuum environment) flows mainly from the micro-heater towards the outer region and that a temperature gradient would be established along fibre's axial direction, we apply the Dirichlet boundary condition to the two outermost fibre end-faces and fix their temperature at 293.15 K.

To test its reliability, convergence test is conducted first for the case of steady-state heat transfer, where we increase the length of the fibre in the model and find out the length beyond which the resultant temperature profile stops changing. As is shown in

Fig. S5, for the fibre length above 1 mm, the temperature profile remains the same. As for the transient calculation, since the 10-pulse temporal evolution is within the time window of less than 1 ms, we set the length of the fibre to 700 μm (given the thermal diffusivity of fused silica, the heat transition length over this time window is about 10 μm).

Section S3. Solid mechanics simulation for the stress-deformation relationship inside the deformed fibre

3.1 Simulation scheme

Conventional numerical simulation for solid mechanics is to map between the constraints with the stress/strain. Typically, the constraints are known as explicit boundary conditions, and the deformation of the structure, together with the associated stress condition would be calculated as the output. However, in our case, constraints upon the deformed fibre are unknown, which are experimentally applied by the tape to fix the fibre with the desired structure. This problem is bypassed by conducting a time-dependent simulation, where the two outermost regions of the fibre are prescribed with rotational displacements. The time-dependent simulation imitates the experimental process of winding the pre-tapered fibre inwards to build the door-shaped structure, which implicitly imposes the boundary constraints in a dynamic process. In the simulation model, the two outermost regions are set as rigid domains. Since the total length of the two regions are kept small (0.001 of the total length), the inaccuracies introduced by this artificiality is trivial.

Solid mechanics simulations are performed in COMSOL Multiphysics. The animation of the time-dependent results can be seen in Movie S9. To approximate a semi-static state, the prescribed displacement is conducted in a rather slow rate. Moreover, after the displacement is finished, the fibre is fixed at its two outer most rigid regions and kept for a considerable period of time for relaxation, during which the deformation and inner stress of the fibre are stabilized. The stress profiles shown in both the main context and this file are the stabilized results of the simulation. Asymmetry of the deformation is considered by setting different rotation radius at the two rigid domains, and the resultant stress distribution is shown in Fig. S9.

3.2 Bending moment analysis

For the deformed structure to relax into and maintain its final state of deformation, equilibrium of moment should be established. The important issue here is to explain the reason why the suspended region is under pure tension, which corresponds to the origin of “pulling force”, and its role in assuring the equilibrium. In Fig S7, equilibriums at two sections of the deformed fibre are schematically illustrated, marked by the solid arrow pair and the dotted arrow pair, respectively. By taking the deformed fibre as a slender beam, the mechanical analysis could be performed under the well-established framework of the beam theory. Therefore, the bending moment at the bending region could be calculated with the following equation:

$$M = \frac{E \cdot I}{\rho} \quad (5)$$

(M: bending moment arising from geometric curvature at cross-section 1 and 2, E: Young's modulus of the fibre material, I: moment of inertia of the fibre cross section. For a circular cross section, I could be calculated with: $I = \frac{\pi \cdot d^4}{64}$, where d denotes the diameter of the circular cross section, ρ: local radius of curvature)

Equilibrium of moment can be evaluated around a point at the neutral layer at position 1 and 2, which is set as the reference point. Considering that cross-section 3 is under pure tension, and that the diameter of the fibre is far smaller compared with the arm of force denoted by r_1 and r_2, the moment generated by the normal stress at Cross-section 3 can be expressed by:

$M = r \times F$ (6)

(M_3: bending moment arising from the tension stress at cross-section 3 with regard to the reference point, F: integral of the normal stress/tension at cross-section 3 as a net force, r: arm of moment, evaluated as the distance between the centers of two cross-sections)

Equation (5) and (6) lead to an approximate expression of the pulling force in the suspended region:

$F = \frac{E \cdot I}{\rho \cdot r}$ (7)

The simulated net force at the suspended region is at ~ mN scale, which is in the same order of magnitude as the result evaluated using Eq. (7), thus solidifying the proposed simulation method. As is exhibited in Fig. S6, the radius of curvature increases from the bending region to the suspended region, while the arm of force corresponding to the reference point in Eq. (6) decreases. The axial evolution of the curvature guarantees the equilibrium of moment in arbitrary section of the deformed fibre, only that while operating the calculation, the moment of inertia should be modified with the shift of the neutral layer.

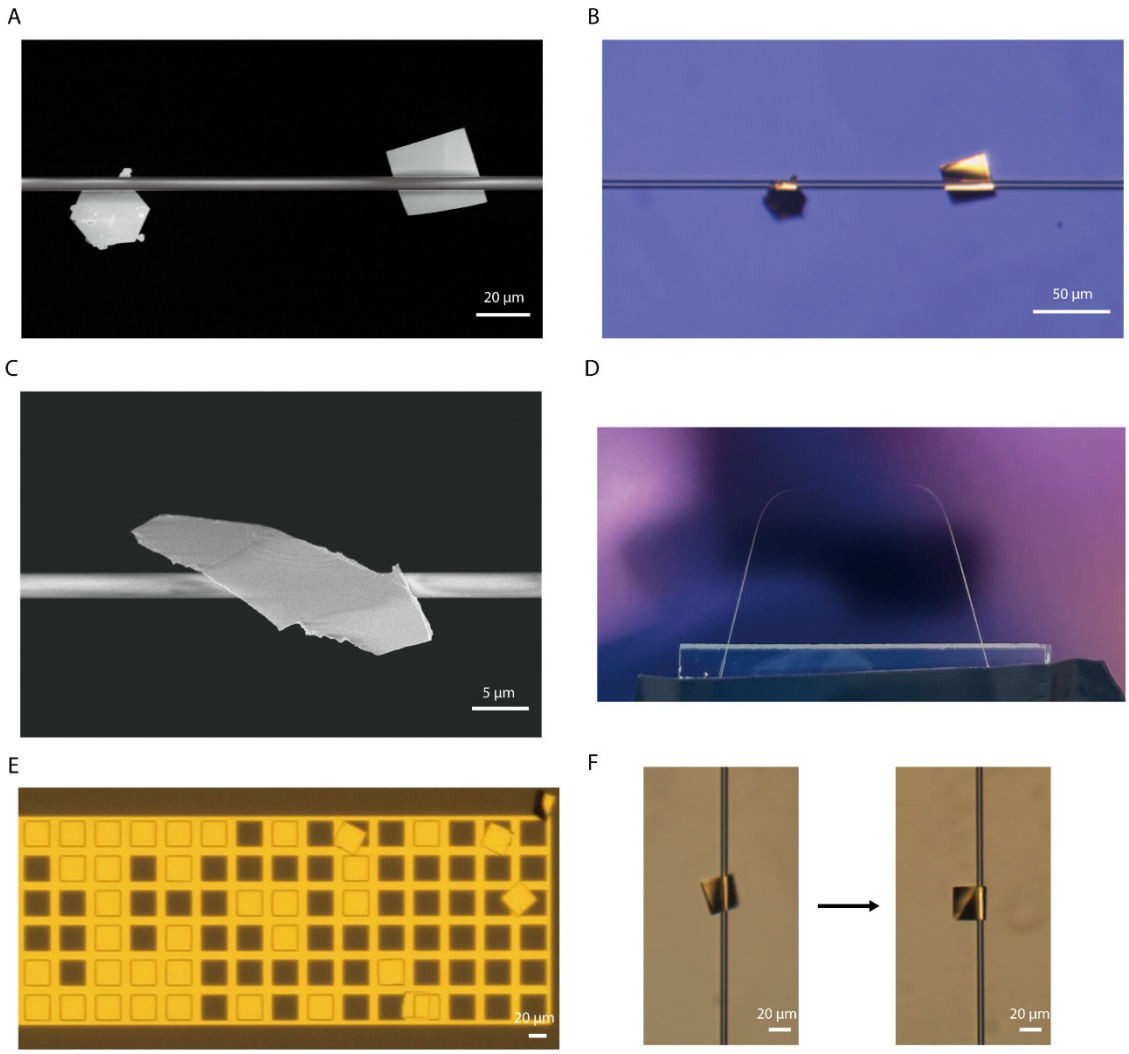

Fig. S1. Preparation of the fibre-plate system. A. SEM image of a chemically fabricated gold plate (left) and an EBL fabricated gold plate (right) attached on an MNF. **B.** Optical microscopic image of **A**. **C**. SEM image of an exfoliated Sb_2Te_3 plate attached on an MNF. **D.** Photo of a fibre deformed in a door-shape structure. The photo is taken by a smart phone (iPhone 13) with the background being an unpolished silicon wafer. **E.** Square-shaped gold plates mass produced using nanofabrication techniques. Geometric parameters including the shape, width, thickness, etc., can be predefined and standardized. After removing the resist layer, the gold plates can be detached from the substrate and be transferred using a fibre probe mounted on a three-dimensional console. **F.** Optical microscopic images of a square gold plate transferred to a pre-tapered fibre, the placement and pose of which can be readily adjusted. Left panel: initial configuration before adjustment. Right panel: plate-fibre configuration after adjustment.

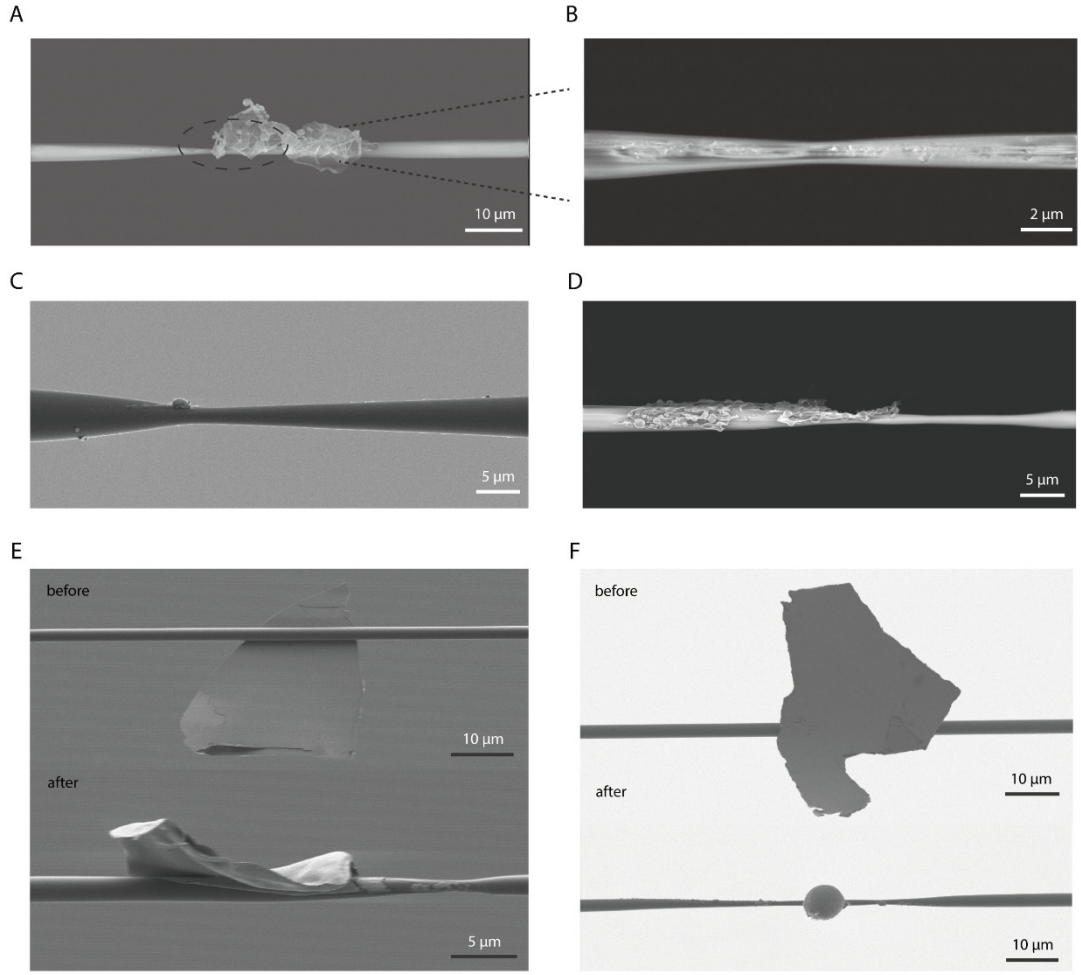

Fig. S2. SEM images of fabricated fibre taper samples. A. SEM image of the fabricated fibre taper before sonication. **B.** Enlarged view of the taper circled in **A** after sonication**. C, D** are SEM images that exhibit asymmetry in the as-fabricated fibre tapers. (Initial fibre diameter: 6.926 µm and 3.034 µm. Waist diameter of the resultant taper: 1.786 µm and 1.025 µm) **E, F** show SEM images before and after the fibre tapering process, with the micro-heater being an exfoliated Sb_2Te_3 plate in **E** and an amorphous gold plate (peeled off from an amorphous gold film) in **F**. (Initial fibre diameter: 1.866 µm and 2.548 µm. Waist diameter of the resultant taper: 805 nm and 863 nm)

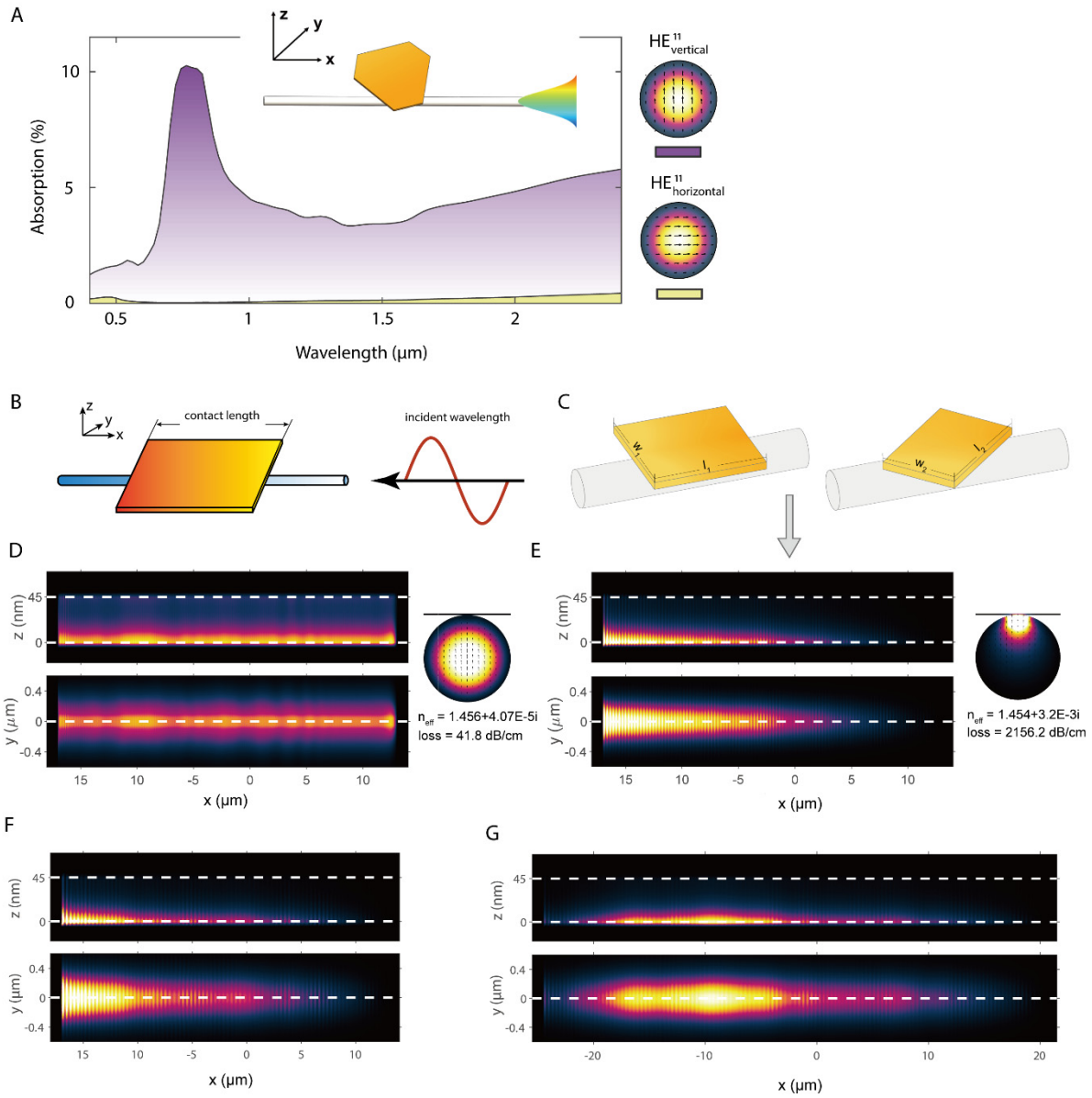

Fig. S3. Calculated absorption of the gold plate-fibre system. A. Absorption spectrum with a broadband incident light source (400-2400 nm). The incident light is chosen to be in the fundamental $HE_{11}^{verticle}$ mode and $HE_{11}^{horizontal}$ mode, which differ by polarization. Inset sketches the simulation model based on the experiment. Apparently, using narrow-band light source resonant with SPPs could bring about the highest thermal efficiency. While considering the sampling randomness of micro-heaters, the adoption of broadband light source possesses the advantage that it would always contain a proportion of light that satisfies the resonance condition. **B.** Schematic of the simulation model adopted to unfold the influence of the plate-fibre contact length and the incident wavelength on the resultant absorption profile. The light propagates in the negative x direction. **C.** Sketch of two different plate-fibre configurations that correspond to the same plate-fibre contact length. The calculated heat source profiles are basically the same (at the same light wavelength), as shown in **E**, which demonstrates the significance of contact length relative to other geometric parameters. **D-G** are calculated absorption profiles with specified simulation set-ups. The input

fibre modes in the four sub-figures are $HE_{11}^{verticle}$ modes. White dashed lines indicate the thickness span of the gold plate and the contact line, respectively. (**D.** Incident wavelength: 532 nm. Contact length: 30 μm. **E.** Incident wavelength: 800 nm. Contact length: 30 μm. **F.** Incident wavelength: 1 μm. Contact length: 30 μm. **G.** Incident wavelength: 1 μm. Contact length: 45 μm.) The right panels in **D** and **E** display the supported mode profiles and the effective refractive index in the hybrid metal-dielectric waveguide at corresponding wavelengths. With the contact length being 30 μm, **D** and **E** represent the off- and on- resonant situations, respectively, while the total heat generation efficiency in the two circumstances would not differ considerably due to the finite contact length and the propagation attenuation.

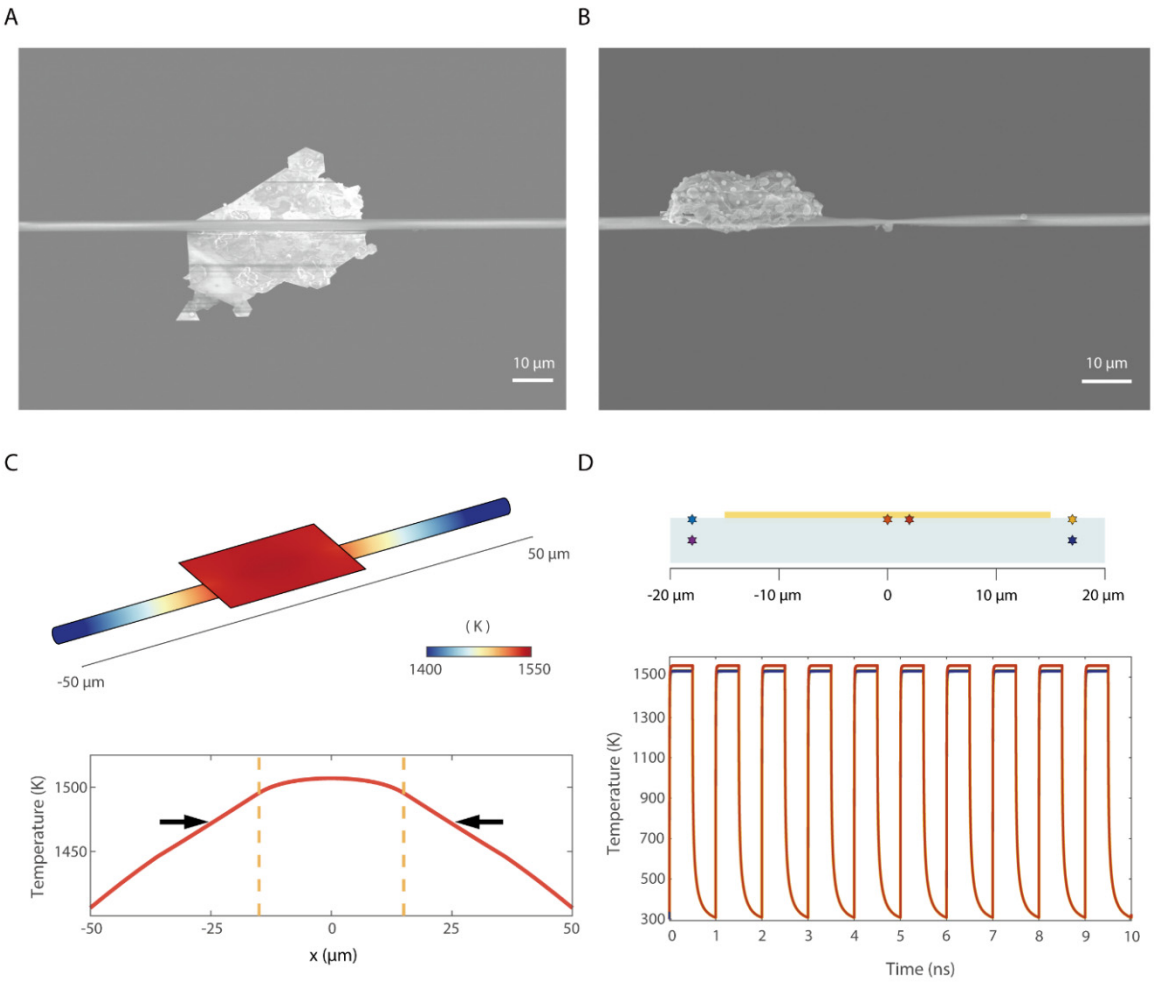

Fig. S4: Fibre taper fabricated with modulated CW light. A. A plate-fibre system before launching the input light. **B.** Ablated gold plate and the fabricated fibre taper. **C.** Temperature profile of the plate-fibre system calculated in the steady-state regime. The heat transfer model is based on the electromagnetic calculation result in Fig. S3. The subplot at the bottom shows the temperature distribution along the fibre-plate touching line (arrows and dotted lines mark the glass transition temperature and the transverse boundary of the gold plate, respectively). **D.** Temperature responses to ten consecutive input pulses (square wave) probed at different sampling points, the position of which are indicated in the upper subplot.

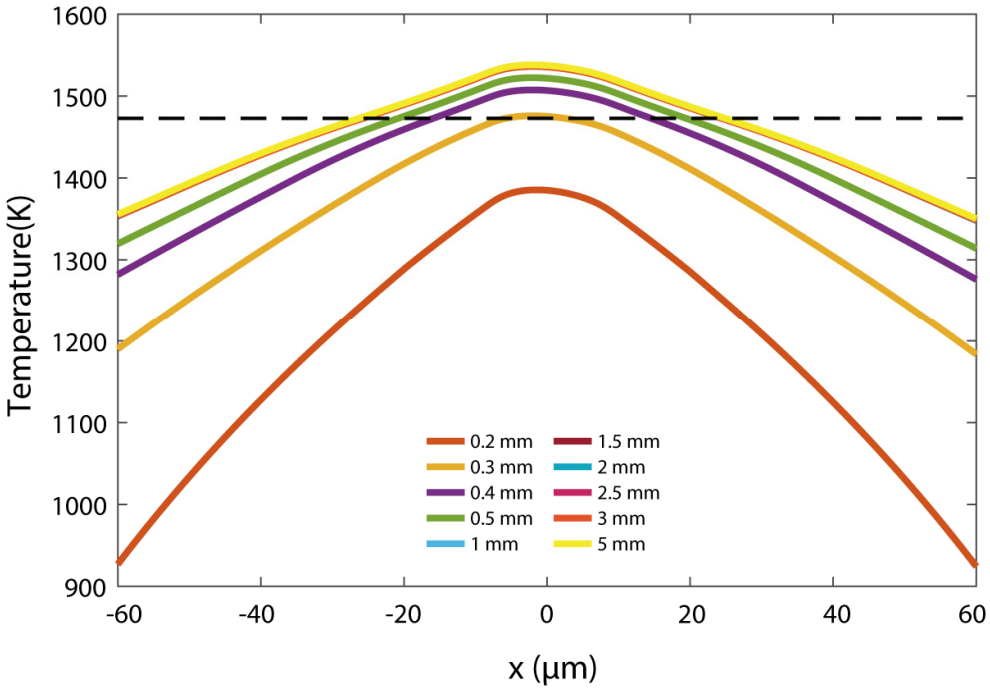

Fig. S5. Convergence test regarding the fibre length adopted in the simulation model. The dashed line indicates the glass transition temperature of fused silica as thermal threshold. For relatively short fibre length, the temperature of the system is underestimated because of the artificially applied boundary condition (293.15 K at two outermost end-faces). With the fibre length increasing, the temperature profile would gradually converge when the balance is achieved between heat input and heat loss (heat conduction along the fibre and thermal radiation towards the environment).

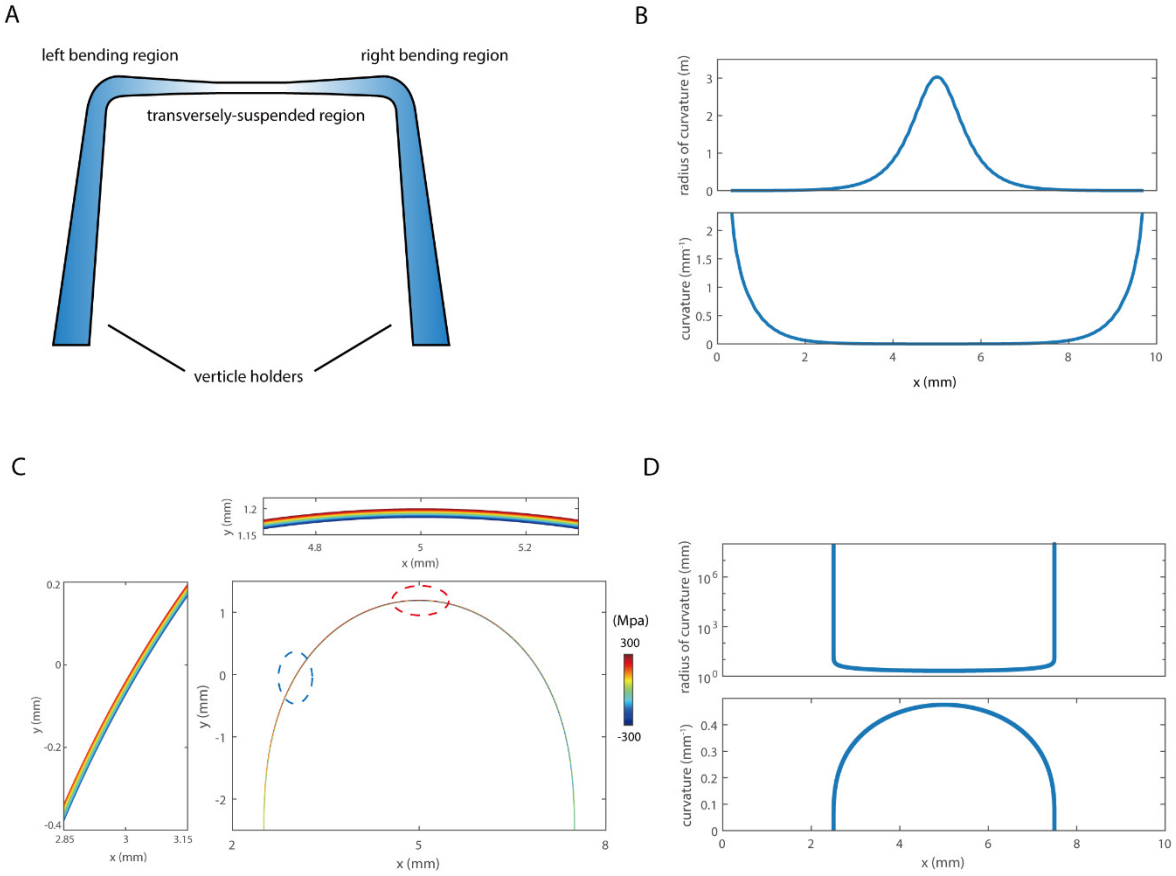

Fig. S6. Characterization of curvature evolution and the corresponding normal stress distribution in deformed silica fibres. A. Schematic of a pre-tapered fibre fixed in a door-shaped manner. **B.** Axial evolution of radius of curvature (unit: m) and curvature (unit: mm^{-1}) of the door-shaped fibre shown in Fig. 6B as quantifiers for degree of bending. While the bending regions feature the largest degree of bending, it gradually decreases towards the middle of the transversely-suspended region, where the micro-heater is usually placed. **C.** Distribution of the axial component of the second Piola-Kirchhoff stress of a circumferentially-deformed fibre (18 μm in diameter). The subplots on the top and the left correspond to the regions marked by red and blue circles, respectively. Both the two regions feature tension at the convex side and compression at the concave side. **D.** Axial evolution of radius of curvature (unit: mm, logarithmic scale along y axis) and curvature (unit: mm^{-1}) of the circumferentially-deformed fibre shown in **C**, the variation trend of which is in contrast with that in **B.**

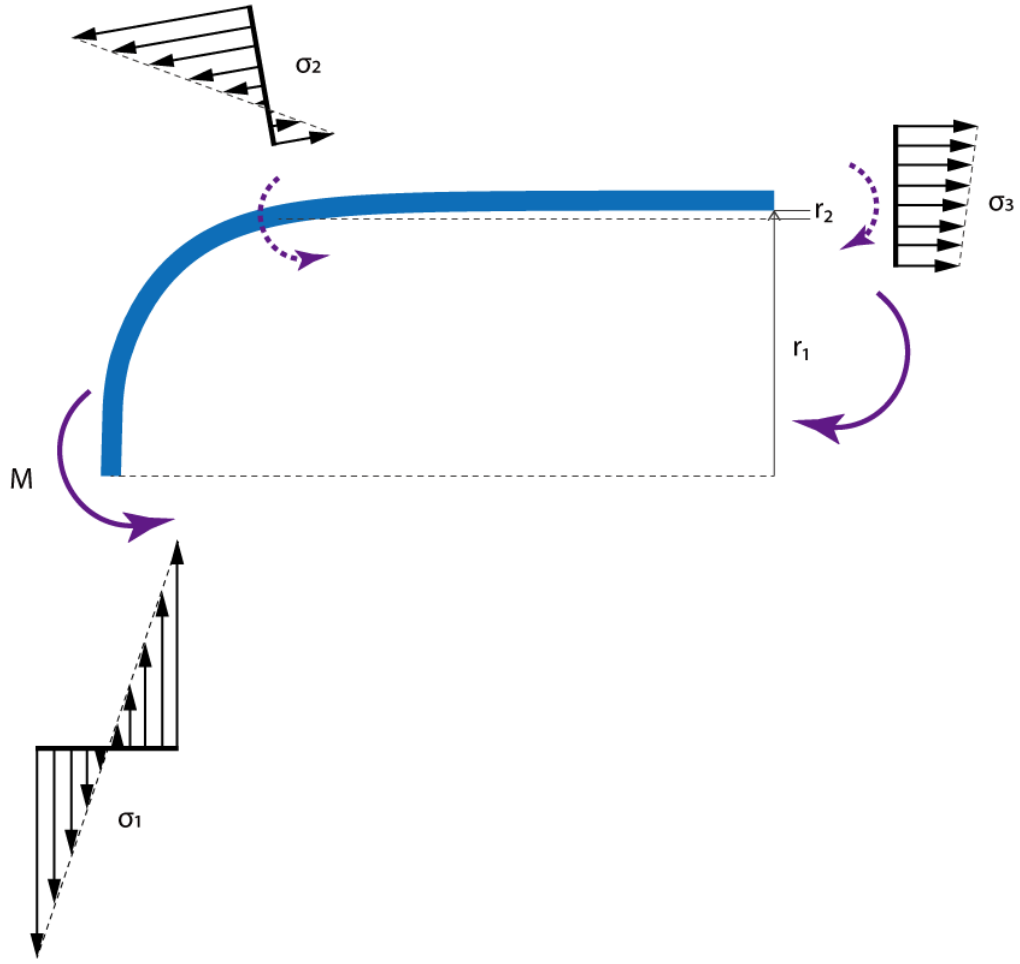

Fig. S7. Schematic of the equilibrium of bending moment inside a deformed fibre. The left section of a deformed fibre is extracted, where the normal stress distributions at three cross-sections are depicted. At the first cross-section, the normal stress distribution (denoted as σ_1) suggests a stress condition similar to that of a cantilever beam under pure bending, with its neutral layer overlapping the geometric center of the beam cross section. As σ axially evolves from the bending region to the suspended region, the slope of the linear stress distribution decreases, with the neutral layer shifting towards the concave side. Equilibrium of moment can be sustained with such axial evolution of normal stress. The two sets of arrows indicate the equilibrium of moment established at two sections of the deformed fibre (solid arrow: the section bounded by the first and third cross-sections, dotted arrow: the section bounded by the second and third cross-sections).

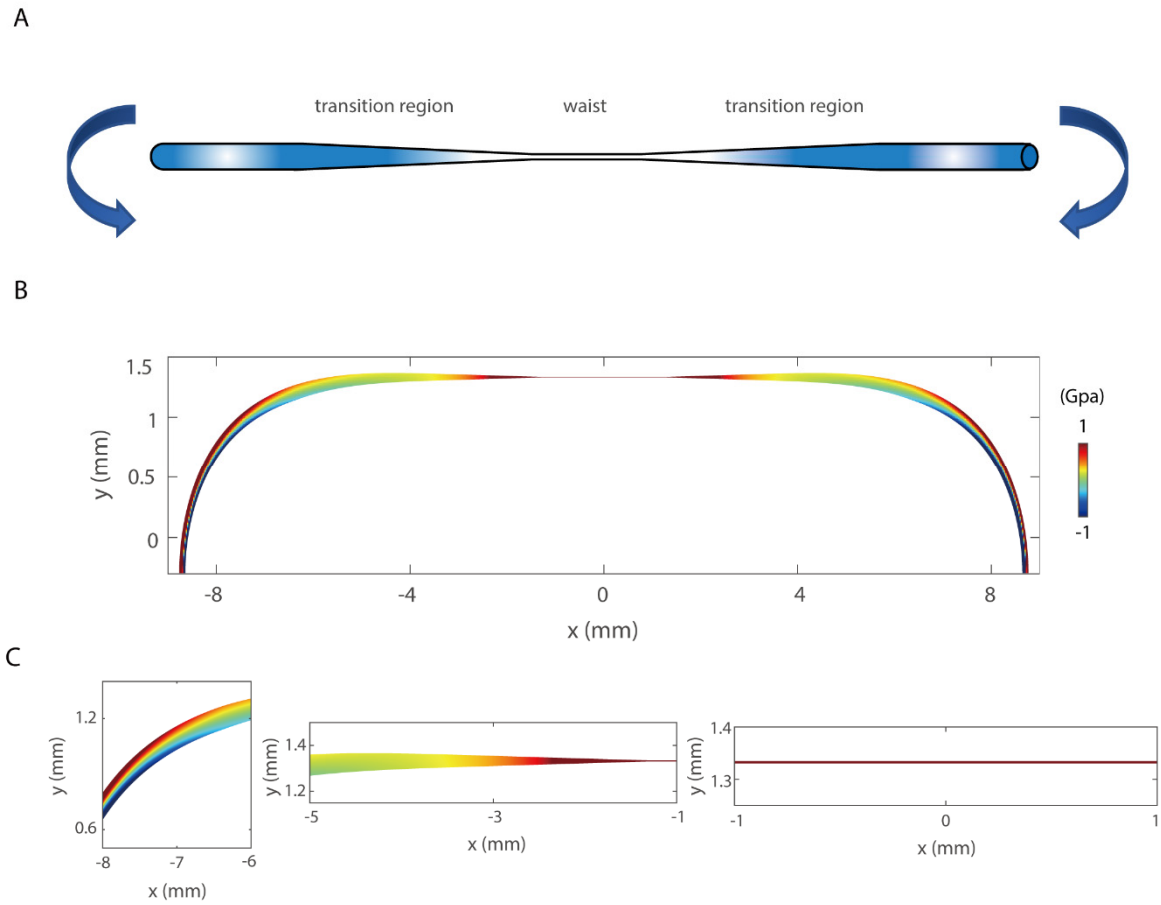

Fig. S8. Stress distribution in a fibre with axially varying diameter. A. Schematic of the pre-tapered fibre in the simulation model, which possesses two linear transition regions. Arrows indicate the prescribed displacement that imitates the experimental process in which the fibre is deformed into a door-shaped structure. **B.** Distribution of the axial component of the second Piola-Kirchhoff stress in a fibre with axially varying diameter (similar to the pre-tapered fibres in experiments). Given that the diameter within the waist region is rather small, y coordinates are scaled by a factor of 2.5 for a better view. **C.** Magnified views of the stress distribution in **B**, corresponding to the waist region, the transition region and the bending connector in the door-shaped structure, respectively.

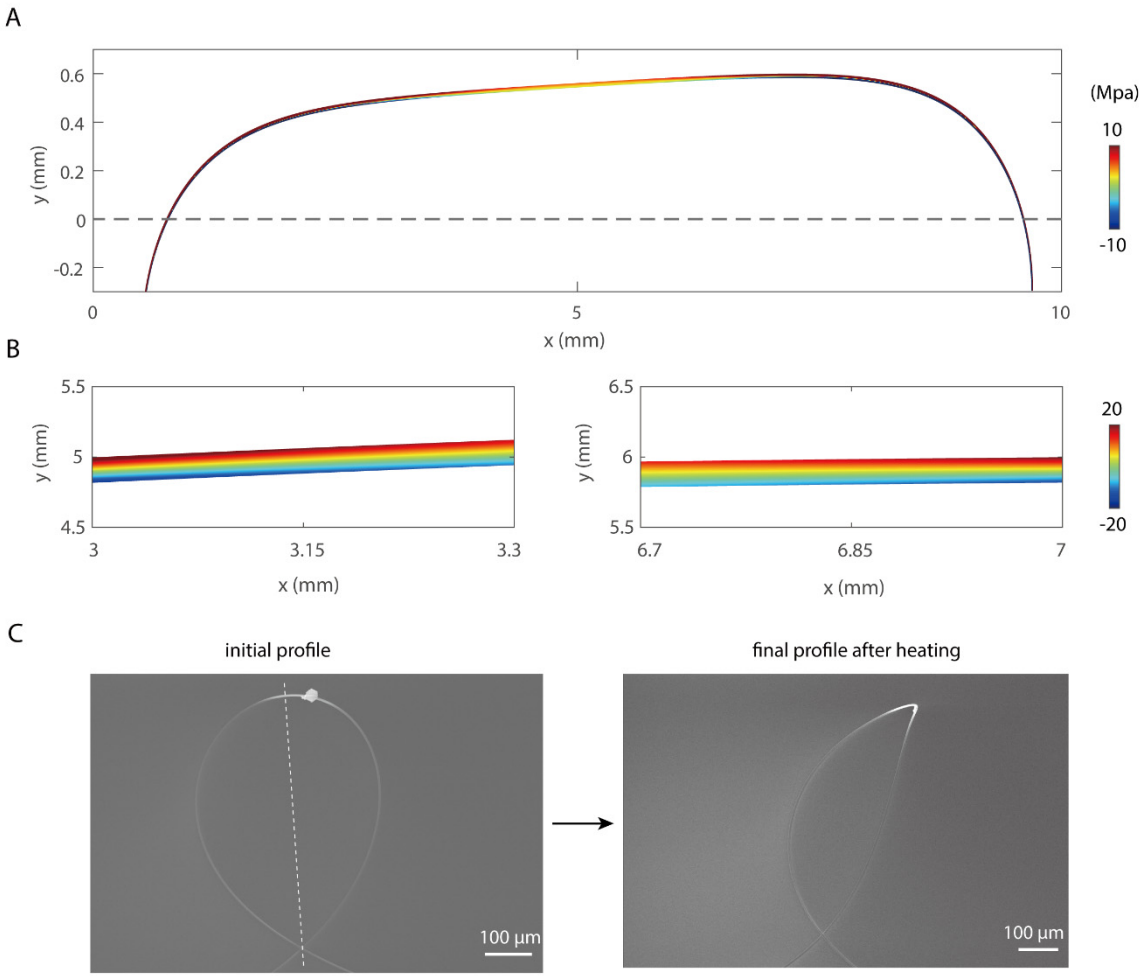

Fig. S9. Influence of geometric asymmetry on stress distribution in the deformed fibre. A. Distribution of the normal stress (axial component of the second Piola-Kirchhoff stress) in an asymmetrically deformed fibre (18 µm in diameter). The y coordinates are scaled by a factor of 2.5. **B** are magnified views of the stress distribution at two mirror positions (axis of symmetry of the undeformed fibre: $x = 5$ mm), suggesting an asymmetric distribution of the bending curvature on the left and right sides. **C.** Profiles of a manually formed fibre loop before and after plasmonic heating. A gold plate is placed to the right of the symmetry axis of the loop (indicated by the white dashed line). After the light is launched into the fibre loop, the hot zone is softened, and what follows is the dynamic behavior of the loop in attempt to release its inner stress favorably in the region near the hot zone. The corresponding video recording can be seen in Movie S10.

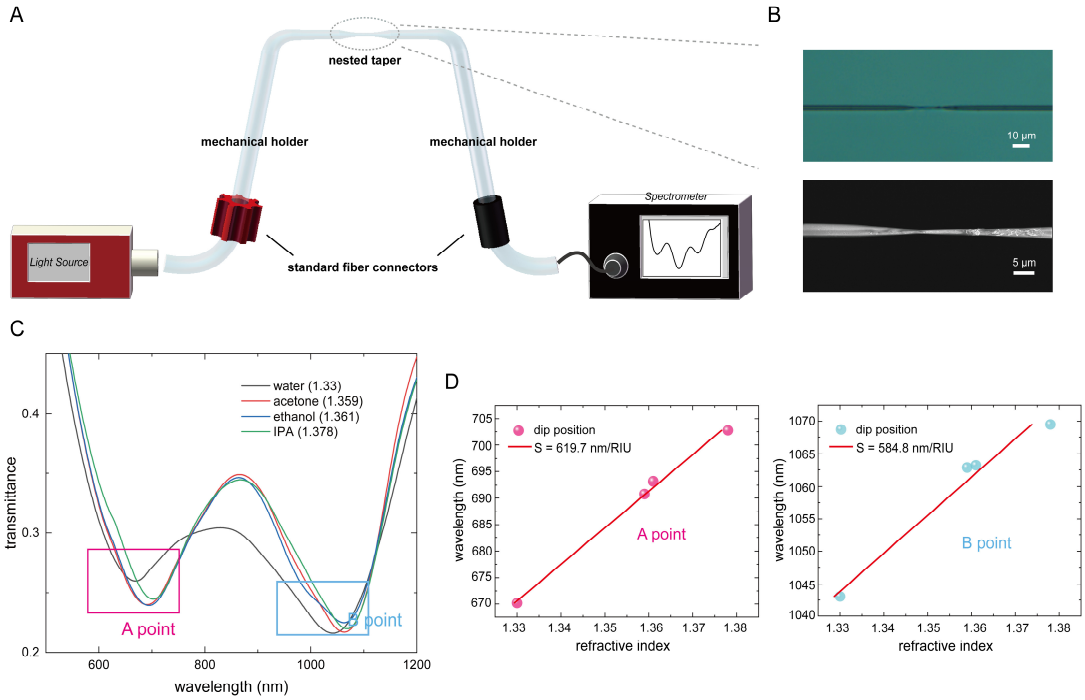

Fig. S10. Demonstration of a fabricated sample used in sensing application. A. Schematic of the sensing experimental set-up. The fabricated taper can be directly integrated into a standard optical path with its two ends (unmodified) connecting other optical components (light source, spectrometer, etc.) via fusion splicing or flange-mounted adaptors. **B.** Optical and SEM images of a fabricated fibre taper in the region circled in **A**. **C.** Measured transmission spectrum of a taper sample (1.1 μm in diameter) in liquid environments with different refractive indexes. Simply by immersing the fabricated sample into test solutions (without additional encapsulation), multimode interference in the nonadiabatic taper would manifest in the transmission spectrum as consecutive dips and peaks, the shift of which could be translated into signals for index sensing. **D.** Relationship between experimental spectra dips and environmental refractive indexes based on **C.**